Atmos. Meas. Tech., 16, 2089–2106, 2023
https://doi.org/10.5194/amt-16-2089-2023

Atmospheric Measurement Techniques
Open Access
EGU

Evaluation of polarimetric ice microphysical retrievals with OLYMPEX campaign data

Armin Blanke[1], **Andrew J. Heymsfield**[2], **Manuel Moser**[3,4], **and Silke Trömel**[1,5]

[1]Department of Meteorology, Institute of Geosciences, University of Bonn, Bonn, 53121, Germany
[2]Mesoscale and Microscale Meteorology Lab (MMM), National Center for Atmospheric Research, Boulder, Colorado, 80307, USA
[3]Institute for Physics of the Atmosphere, University Mainz, Mainz, 55099, Germany
[4]Institut für Physik der Atmosphäre, Deutsches Zentrum für Luft- und Raumfahrt, Oberpfaffenhofen, 82234, Germany
[5]Laboratory for Clouds and Precipitation Exploration, Geoverbund ABC/J, Bonn, 53121, Germany

Correspondence: Armin Blanke (armin.blanke@uni-bonn.de)

Received: 22 December 2022 – Discussion started: 13 January 2023
Revised: 14 March 2023 – Accepted: 15 March 2023 – Published: 20 April 2023

Abstract. Polarimetric microphysical retrievals reveal a great potential for the evaluation of numerical models and data assimilation. However, the accuracy of ice microphysical retrievals is still poorly explored. To evaluate these retrievals and assess their accuracy, polarimetric radar measurements are spatially and temporally collocated with in situ aircraft measurements obtained during the OLYMPEX campaign (Olympic Mountain Experiment). Retrievals for ice water content (IWC), total number concentration N_t, and mean volume diameter D_m of ice particles are assessed by comparing an in situ dataset obtained by the University of North Dakota (UND) Citation II aircraft with X-band Doppler on Wheels (DOW) measurements. Sector-averaged range height indicator (RHI) scans are used to derive vertical profiles of microphysical retrievals. The comparison of these estimates with in situ data provides insights into strengths, weaknesses, and the accuracy of the different retrievals and quantifies the improvements in polarimetry-informed retrievals compared to conventional, non-polarimetric ones. In particular, the recently introduced hybrid ice water content retrieval exploiting reflectivity Z_H, differential reflectivity Z_{DR}, and specific differential phase K_{DP} outperforms other retrievals based on either (Z_H, Z_{DR}) or (Z_H, K_{DP}) or non-polarimetric retrievals in terms of correlations with in situ measurements and the root mean square error.

1 Introduction

Polarimetric microphysical retrievals bear great potential for data assimilation and the evaluation of numerical models, however, their exploitation is still in its infancy. For instance, Trömel et al. (2021) demonstrated the potential of using polarimetric observations and retrievals to evaluate and improve microphysical parameterizations. Pioneering work by Carlin et al. (2016) revealed the benefits of assimilating polarimetric microphysical retrievals. Similar work is currently underway in Germany. Reimann et al. (2021) took a first step towards assimilating polarimetric variables into the ICOsahedral Nonhydrostatic (ICON) model (Zängl et al., 2015) via adapting microphysical retrievals for their application to observations of the polarimetric C-band radar network of the German national meteorological service.

Ryzhkov et al. (1998) pointed to the limited database to identify the main reasons for the differences between individual in situ measurements and polarimetric retrievals. In fact, the in-depth evaluation of retrievals requires extensive airborne in situ cloud particle measurements over polarimetric radar sites using, e.g., so-called optical array probes (OAPs) collected during field campaigns. However, these are substantial high budget and provide data only along flight trajectories. Hogan et al. (2006) introduced an ice water content (IWC) based on radar reflectivity Z and atmospheric temperature T. Tian et al. (2016) evaluated its performance along with that of a mean volume diameter D_m retrieval with air-

craft in situ data from the Bow Echo and Mesoscale Convective Vortex Experiment (BAMEX; Davis et al., 2004). They observed an overestimation of the mean Hogan IWC retrieval compared to in situ measurements ($1.52\,\mathrm{g\,m^{-3}}$ vs. $1.25\,\mathrm{g\,m^{-3}}$) and a correlation of 0.55. Similarly the mean retrieved D_m showed an overestimation (2.08 mm vs. 1.77 mm) and a low correlation of 0.27.

One reason for the bad performance of non-polarimetric retrievals is that the horizontal reflectivity Z_H in snow is approximately proportional to the fourth moment of the particle size distribution (PSD) (Hu and Ryzhkov, 2022); hence Z_H is insensitive to small particles, whereas other moments, such as the IWC, are sensitive to the small particle contributions. In contrast, specific differential phase K_DP is proportional to the first moment of the PSD and thus the whole spectrum is considered. However, K_DP strongly depends on the aspect ratio and orientation of the particles, necessitating prior knowledge of these parameters. Aydin and Tang (1997) proposed for IWC estimation the combination of K_DP and differential reflectivity Z_DR because their ratio is not affected by the variability in orientation and particle aspect ratio (Ryzhkov et al., 2018). Another set of polarimetric relations to quantify snow properties was derived by Bukovčić et al. (2018) exploiting Z_H and K_DP. More recently, Carlin et al. (2021) suggested a hybrid application for estimating IWC by combining the complementary strengths and optimal ranges of the IWC retrievals following Bukovčić et al. (2018) and Ryzhkov and Zrnić (2019). Apart from IWC retrievals, polarimetric retrieval relations have been suggested for D_m and total number concentration of ice particles per unit volume N_t based on approaches utilizing combinations of three or two polarimetric variables, always including K_DP (Ryzhkov et al., 2018; Bukovčić et al., 2020). To evaluate the quality of polarimetric retrievals, approaches based on in situ and/or ground-based measurements were pursued.

Nguyen et al. (2019) proposed a methodology to retrieve IWC using Z_DR and K_DP from X-band dual-polarization airborne radar data. This algorithm was found to be superior to power-law fits using Z compared to others because Z_DR minimizes the dependence of IWC on variations in ice particle shape and orientation. An evaluation with in situ data from the High Altitude Ice Crystal – High Ice Water Content (HAIC-HIWC) field campaign revealed that the additional use of Z_DR reduced the root mean square difference by 6 % and the bias by 15 % on average compared to retrievals using K_DP only.

Several noise-reducing techniques for reconstructing average vertical profiles from radar data have been proposed and used in the literature (Table 1). They are based on plan position indicator (PPI) or range height indicator (RHI) scans using single or multiple elevations. However, polarimetric and especially the phase-based radar measurements may be noisy in ice and snow and even more near the cloud top. As a consequence, it is beneficial to reduce their statistical noise before the calculation of microphysical retrievals. For instance columnar vertical profiles (CVPs; Murphy et al., 2020) represent local average vertical profiles that can be calculated at any distance from the radar using all elevation scans. Murphy et al. (2020) applied the microphysical retrievals by Ryzhkov et al. (2018) to CVPs and tracked airborne in situ measurements to exploit them for evaluation. Overall, newly developed polarimetric retrievals show good promise in quantitatively estimating IWC, N_t, and D_m. However, Murphy et al. (2020) especially revealed deficiencies near the melting layer (ML), resulting in, e.g., a pronounced underestimation of D_m in these regions. Also using in situ measurements from aircraft, alternative retrieval methods were recently tested. Kedzuf et al. (2021) validated the accuracy of statistical polarimetric retrieval methods designed for pristine ice and aggregates, and Dunnavan et al. (2022) evaluated aspect ratio retrievals (Matrosov et al., 2020).

This study exploits measurements obtained during the Olympic Mountain Experiment (OLYMPEX) field campaign conducted from November 2015 to February 2016 on the Olympic Peninsula of Washington State, USA (Houze et al., 2017). During OLYMPEX, the University of North Dakota's (UND) Cessna Citation II science aircraft equipped with an advanced in situ cloud payload performed overpasses over the National Science Foundation (NSF)-funded Doppler on Wheels (DOW) radar. We focus on the evaluation of radar-derived IWC, D_m, and N_t. Our accuracy assessments are based on two key aspects: (1) the matching of ground-based polarimetric radar data with airborne in situ cloud particle measurements in time and space and (2) a noise-reducing averaging of the polarimetric radar measurements in the ice phase. Throughout OLYMPEX, the DOW X-band radar performed sequences of RHI scans in azimuthal sectors of 22°, which motivated us to introduce the RHI sector vertical profile (RSVP) technique to determine vertical profiles of polarimetric variables within specified sectors in azimuth and range.

The major objective of this study is to exploit the OLYMPEX campaign data for the accuracy assessment of the most recent microphysical retrievals and emphasize at the same time the benefits of X-band radars for microphysical studies.

The paper is organized as follows. Section 2 introduces the polarimetric remote sensing observations and airborne in situ measurements used. Section 3 summarizes the microphysical retrievals considered, while the RSVP methodology and the matching with aircraft measurements are detailed in Sect. 4. Evaluation results are presented in Sect. 5 followed by a discrepancy analysis in Sect. 6. A summary of key findings and a comprehensive discussion of all results are provided in Sect. 7.

2 The OLYMPEX campaign database

The OLYMPEX ground validation field campaign (Houze et al., 2017), conducted in the Pacific Northwest, aimed at val-

Table 1. Overview of areal averaging techniques to derive quasi-vertical profiles of polarimetric radar variables.

Methodology	Acronym	Scan strategy	Used azimuth	Used elevations	Citation
Quasi-vertical profile	QVP	PPI	360°	Single high	Ryzhkov et al. (2016)
Range-defined QVP	RD-QVP	PPI	360°	Multiple	Tobin and Kumjian (2017)
Columnar vertical profile	CVP	PPI	Sector	Multiple	Murphy et al. (2020)
Enhanced vertical profile	EVP	PPI	Sector	Multiple	Bukovčić et al. (2017)
Slanted vertical profile	SVP	PPI	Sector	Single low	Bukovčić et al. (2017)
Range height indicator QVP	R-QVP	RHI	Fixed	Multiple	Allabakash et al. (2019)

idating rain and snow measurements in midlatitude frontal systems and to further develop the Global Precipitation Measurement (GPM) mission satellite algorithms for precipitation estimation. Of the broad variety of ground instruments, including several radars and airborne instruments, the DOW in conjunction with the in situ aircraft measurements of the Citation II is appropriate for our evaluation purposes.

2.1 Polarimetric data from X-band radar DOW

The DOW radar (Wurman et al., 1997), placed within Chehalis Valley at Lake Quinault (47.48° N, 123.86° W; at 64 m altitude), Washington, and operated by the Center of Severe Weather Research (CSWR), is installed on a mobile truck. The polarimetric dual-frequency X-band radar operated with a range of 59.96 km and a radial resolution of 75 m and used two independent transmitters at frequencies of ~ 9.55 GHz and ~ 9.40 GHz (Houze et al., 2018). In this study, we exclusively utilize the latter frequency as only measurements of the lower frequency were available after 12 November 2015. More detailed information on the DOW radar can be found in Houze et al. (2018).

The DOW's 10 min scanning schedule includes plan position indicator (PPI) scans for the azimuthal sector between 39.2 and 83.6° at six elevations between 2.8 and 11° and a series of 22 range–height indicators (RHIs) for the azimuthal sector between 50.4 and 71.4° in equidistant intervals of 1° and elevations ranging from 0 to 71°. For the evaluation of polarimetric ice microphysical retrievals, we focus in this study on the sector RHIs. All datasets utilized (Petersen et al., 2018), including a new version of the DOW data with improved calibration (Houze et al., 2018; doi: https://doi.org/10.5067/GPMGV/OLYMPEX/DOW/DATA201), were downloaded from the Global Hydrology Resource Center (GHRC) Distributed Active Archive Center (DAAC). As a cross-check, we followed Ryzhkov and Zrnić (2019) and verified whether the expected Z_H–Z_{DR} relationship for X-band in rain is fulfilled and made adjustments of Z_{DR} if necessary. Accordingly, a Z_{DR} correction was applied to all data used, with a larger correction required for measurements in November than in December (on average 0.38 dB vs. 0.19 dB).

Specific differential phase K_{DP}, defined as half the range derivative of differential propagation phase shift Φ_{DP}, is estimated following Vulpiani et al. (2012). For processing efficiency, the derivative of Φ_{DP} is approximated using low-noise Lanczos differentiators (Holoborodko, 2008). Since K_{DP} is inversely proportional to the radar wavelength, more reliable estimates can be expected at X-band compared to C- or S-band with according benefits also for microphysical retrievals. Only data with a cross-correlation coefficient ρ_{hv} above 0.7 are used for the K_{DP} estimation in order to reduce the impact of noisy and non-meteorological contamination.

2.2 In situ sensors and observations

The in situ microphysical cloud measurements during the OLYMPEX campaign have been acquired with the University of North Dakota (UND) Cessna Citation II airplane, which was equipped with an enhanced instrumental payload, including the 2D stereo imaging probe (2D-S; SPEC Inc, USA) and the high-volume precipitation spectrometer (HVPS; SPEC Inc, USA). Both instruments provide shadowgraphs of cloud particles. The 2D shadow images of hydrometeors are generated as the particles penetrate through the sampling area of the particle imagers. A detailed description of the 2D-S and HVPS operating principles, uncertainties, and limitations can be found in Lawson et al. (2006), Baumgardner et al. (2017), and Moser et al. (2023). Note that the data recorded by the 2D-S and HVPS differ in sampling volume size and pixel resolution. The 2D-S is equipped with 128 pixels of 10 µm resolution each, which allows imaging particles from 10 µm to 1.28 mm in size. With the larger pixel resolution provided by the HVPS of 150 µm, imaging of hydrometeors from 150 µm to 3.25 cm is enabled. Here, the datasets of the horizontally oriented HVPS and the horizontally oriented part of the 2D-S processed by Heymsfield et al. (2018) were combined with a switch-over size at 1000 µm; i.e., particles smaller than 1000 µm are sized by the 2D-S and larger particles by the HVPS. Standard processing and correction options with SODA (software for OAP data analysis, provided by Aaron Bansemer, National Center for Atmospheric Research/University Corporation for Atmospheric Research; Bansemer, 2023) were applied including shattering and dead-time corrections. For a better comparability of the in situ measurements with the according radar-based retrievals of IWC, D_m, and N_t, only particles larger than 100 µm are considered because of the sensitiv-

ity of weather surveillance radars (Ryzhkov et al., 2020) and uncertainties in probe data (Poellot and Bansemer, 2017; Baumgardner et al., 2017). With the particle size distribution (PSD) given by Heymsfield et al. (2018), D_m, IWC, and N_t for particles between 100 µm and 3 cm are calculated. In order to derive N_t, the number concentration for each particle size bin is added up.

The different relations between measures of particle sizes used in the radar community and those derived from in situ measurements must be considered in their comparison. Radar-based retrievals mostly provide the mean volume diameter D_m as a parameter for the size of the particles, which is defined as the ratio of the fourth to the third moment of the PSD:

$$D_\mathrm{m} = \frac{\int D^4 N(D)\mathrm{d}D}{\int D^3 N(D)\mathrm{d}D}, \tag{1}$$

where D is the equivolume diameter. It should be noted that D_m is very close to the median volume diameter D_0. Assuming that the PSD follows a gamma distribution with shape parameter μ (Ulbrich, 1983), we obtain

$$D_\mathrm{m} = \frac{4+\mu}{3.67+\mu} D_0. \tag{2}$$

Instead of D_m, the aircraft microphysical probes usually measure either the median mass diameter D_mm or the median volume diameter D_mv of the distribution of maximal particle dimension (Hu and Ryzhkov, 2022), which is given by

$$D_\mathrm{max} = D\varphi^{-1/3}, \tag{3}$$

where φ is the particle aspect ratio. For a gamma size distribution and taking Eq. (3) into account, we yield

$$D_\mathrm{mm} = \frac{2.67+\mu}{4+\mu} \frac{D_\mathrm{m}}{\varphi^{1/3}}, \tag{4a}$$

$$D_\mathrm{mv} = \frac{3.67+\mu}{4+\mu} \frac{D_\mathrm{m}}{\varphi^{1/3}}, \tag{4b}$$

with Eq. (4a) assuming particle density being inversely proportional to its size. Assuming $\varphi = 0.6$ and an exponential distribution ($\mu = 0$), the following two D_m relationships (Hu and Ryzhkov, 2022) are obtained:

$$D_m \approx \frac{D_\mathrm{mm}}{0.79} \tag{5a}$$

and

$$D_m \approx \frac{D_\mathrm{mv}}{1.09}. \tag{5b}$$

These relations enable the direct comparison between the in situ measurements with the radar-based D_m retrievals, with the median mass size D_mm derived in situ utilized in our study to obtain D_m. The IWC is estimated by using a mass–dimension relation between mass m and size given by

$$m = aD_\mathrm{max}^b, \tag{6}$$

with $a = 0.0121$ kg per m^b $b = 1.9$, and D_max the diameter of the minimum enclosing circle of the projected 2D image. We followed Chase et al. (2018) by adopting Eq. (6) and parameters a and b from Brown and Francis (1995) and modifying them considering the particle size definition by Hogan et al. (2012). Even though parameters a and b of the mass–dimension relationship vary with the environmental conditions and particle shapes (Baker and Lawson, 2006), constant standard parameters are used in this study which reasonably represent the mean ice water content, especially for ice crystal aggregates. Tridon et al. (2019) confirmed that the aggregates observed during OLYMPEX can mostly be described by a quite narrow range of mass–size relations. In single situations with large aggregates or intense riming processes, however, the fixed parametrization may underestimate the ice water content (see also Heymsfield et al., 2023).

In addition to the quantitative information provided by the 2D-S and HVPS, high-resolution in situ particle imagery data from the cloud particle imager (CPI; SPEC Inc, USA) can be used to accurately identify particle types and characteristics. Only with the CPI is it possible to directly monitor supercooled liquid water (SLW) droplets of micron size attached to ice particles and thus diagnose riming unambiguously and estimate the degree of riming.

The Rosemount icing detector (RICE; Baumgardner and Rodi, 1989) mounted on the Citation II is used as a supporting probe to detect the presence of SLW mandatory for riming (Vogel and Fabry, 2018). The RICE oscillates at a constant frequency, but when supercooled droplets freeze on its surface, the frequency of vibration decreases. Once accumulated ice exceeds a certain threshold, the probe tip is briefly heated to remove accreted ice. Data are available again as soon as the probe temperature has stabilized (Heymsfield and Miloshevich, 1989).

3 Radar-based microphysical retrievals

This section summarizes the most recent polarimetric and a suite of conventional non-polarimetric ice microphysical retrievals for IWC, N_t, and D_m considered and assessed in this study. Two conventional D_m retrievals derived from statistical relations between particle sizes and reflectivity expressed in linear scale ($Z_\mathrm{h} = 10^{0.1Z_\mathrm{H}}$; in units of mm^6 m^{-3}) are used in our analysis. The first relation introduced by Skofronick-Jackson et al. (2019) is based on a power law between D_m (mm) and Ku-band Z_h fitted to data from the GPM Cold Season Precipitation Experiment (GCPEx) campaign (Skofronick-Jackson et al., 2015) conducted in Canada:

$$D_\mathrm{m}^\mathrm{I}(Z_\mathrm{h}) = 1.45{Z_\mathrm{h}}^{0.25}. \tag{7}$$

Matrosov et al. (2019) introduced another power-law relation derived from Z_h data of ground-based S-band radar and aircraft in situ calculated D_{mv} obtained during the Indirect and Semi-Direct Aerosol Campaign (ISDAC) in Alaska (Maahn et al., 2015). Assuming $\varphi = 0.6$ and using Eq. (5b), it follows that

$$D_m^{II}(Z_h) = \frac{1}{1.09} \cdot \left(1.15 {Z_h}^{0.271}\right). \quad (8)$$

This equation differs from Eq. (5) in Murphy et al. (2020) showing, due to a typo, the reciprocal multiplier when converting D_{mm} to D_m.

Since Z_H-based D_m retrievals are disproportionally weighted by a few large particles, polarimetric K_{DP}-based retrievals have a great potential to provide more accurate estimates. Additionally, such estimators use the key advantage that K_{DP} is not affected by attenuation and not biased by noise and radar miscalibration. To retrieve a polarimetric D_m from K_{DP} and Z_{dp}, where $Z_{dp} = Z_h - Z_v$ is the reflectivity difference at horizontal and vertical polarization in linear scale, as proposed in Ryzhkov et al. (2018) and Ryzhkov and Zrnić (2019), we use

$$D_m(Z_{dp}, K_{DP}) = -0.1 + 2.0\left(\frac{Z_{dp}}{K_{DP}\lambda}\right)^{1/2}, \quad (9)$$

where K_{DP} is in degrees per kilometer, Z_{dp} is in millimeters to the power of six per cubic meter ($mm^6\,m^{-3}$), and the radar wavelength λ is in millimeters. This estimator is largely immune to variations in ice particle orientation and shape but has the inherent deficiency of being impacted by the degree of riming; therefore it is supposed to be more appropriate for lower-temperature regions where riming is less likely. As an alternative, Bukovčić et al. (2018, 2020) use Z_h and K_{DP} to retrieve

$$D_m(Z_h, K_{DP}) = 0.67\left(\frac{Z_h}{K_{DP}\lambda}\right)^{1/3}. \quad (10)$$

Unlike $D_m(Z_{dp}, K_{DP})$, however, this retrieval is not immune to the variability in particle orientation and shape, and a strength of this $D_m(Z_h, K_{DP})$ estimate is that it does not depend on density and is therefore not affected by the degree of riming.

Similarly to the aforementioned D_m retrievals, IWC retrievals can also be derived in a purely empirical fashion through the utilization of power laws. Hogan et al. (2006) introduced an expression which related in situ measured IWC (in $g\,m^{-3}$) to reflectivity (in dBZ) at various frequencies (e.g., 3 GHz) and temperature T (in °C) in the European Cloud Radiation Experiment (EUCREX) derived in the Rayleigh approximation:

$$\log_{10}\left(\mathrm{IWC}^{I}(Z_H, T)\right) = 0.06 Z_H - 0.0197T - 1.7. \quad (11)$$

They also exploited the $\mathrm{IWC}^{I}(Z_H, T)$ to evaluate the mesoscale version of the Met Office Unified Model. However, the IWC relationship implicit in the models' parameterization (see Hogan et al., 2006, for details) is

$$\log_{10}\left(\mathrm{IWC}^{II}(Z_H, T)\right) = 0.06 Z_H - 0.0212T - 1.92. \quad (12)$$

Nguyen et al. (2019) proposed two more empirical but polarimetric IWC retrievals via optimal fitting parameters, exploiting aircraft measurements from a polarimetric side-pointing X-band radar and measured IWC by in situ probes obtained during HAIC-HIWC. The two retrievals either utilize K_{DP} only or include additionally the differential reflectivity Z_{dr} expressed in linear scale ($Z_{dr} = 10^{0.1 Z_{DR}}$):

$$\mathrm{IWC}(K_{DP}) = 0.903 K_{DP} + 0.319 \text{ and} \quad (13)$$

$$\mathrm{IWC}^{I}(Z_{dr}, K_{DP}) = \frac{0.136 K_{DP} + 0.037}{1 - Z_{dr}^{-1}}. \quad (14)$$

Z_{dr} is set to 1.15 (Ryzhkov et al., 1998) when Z_{dr} falls below this threshold. Ryzhkov et al. (1998) also demonstrated that K_{DP} is sensitive to the aspect ratio φ and orientation of the particles, whereas IWC is not, requiring additional knowledge about the particles. Accordingly, the estimator $\mathrm{IWC}(K_{DP})$ is highly affected by variations in φ and/or orientation, whereas the inclusion of Z_{dr} in $\mathrm{IWC}^{I}(Z_{dr}, K_{DP})$ reduces these dependences. The observational study by Nguyen et al. (2019) demonstrated that their empirical relation $\mathrm{IWC}^{I}(Z_{dr}, K_{DP})$ is very close to the theoretical IWC relation by Ryzhkov et al. (2018):

$$\mathrm{IWC}^{II}(Z_{dr}, K_{DP}) = 4 \times 10^{-3}\left(\frac{K_{DP}\lambda}{1 - Z_{dr}^{-1}}\right). \quad (15)$$

The latter exploits the inherent information of Z_{dr} about the shape and the orientation of particles. Similar to Eq. (9), $\mathrm{IWC}^{II}(Z_{dr}, K_{DP})$ is practically insensitive to the shape and orientations of the ice particles because the numerator and denominator are proportionally impacted and thus the ratio is not affected.

In the absence of a birdbath scan in the scan schedule (as is, e.g., the case for the operational radar networks in the USA), ensuring high Z_{dr} accuracy is often difficult. Bukovčić et al. (2018, 2020) introduced a generalized relation for IWC,

$$\mathrm{IWC}(Z_h, K_{DP}) = \frac{10.2 \times 10^{-3}}{(F_0 F_S)^{0.66}} (K_{DP}\lambda)^{0.66} {Z_h}^{0.28}, \quad (16)$$

which is immune to Z_{dr} miscalibrations and where F_0 is the orientation factor as a function of the width of the canting angle distribution σ and F_S the shape factor determined by φ. The relation in Eq. (16) produces

$$\mathrm{IWC}(Z_h, K_{DP}) \approx 0.31 {K_{DP}}^{0.66} {Z_h}^{0.28}, \quad (17)$$

for $\sigma = 0°$, $\varphi = 0.65$, and $\lambda = 32$ mm. In contrast to Eq. (10), however, the $\mathrm{IWC}(Z_h, K_{DP})$ retrieval is sensitive to the density of the particles and thus the degree of riming.

The combined application of Eq. (15) in regions where $Z_{DR} > 0.4$ dB and Eq. (17) elsewhere, as suggested by Carlin et al. (2021), leverages the strengths of both formulas and is denoted as IWC_{Carlin} estimator in the following.

Estimating snow concentration N_t is a challenging task, and it is almost impossible to derive it with acceptable accuracy from single-polarization radar measurements because of the wide variety of ice and snow habits and their microphysical properties. A polarimetric retrieval for the logarithm of the total number concentration of ice particles N_t (in L^{-1}) following Ryzhkov et al. (2018) and Ryzhkov and Zrnić (2019) is estimated by

$$\log_{10}\left(N_t(Z_H, Z_{dp}, K_{DP})\right) = 0.1 Z_H - 2\log_{10}\gamma - 1.33, \tag{18a}$$

with

$$\gamma \approx 0.78\left(\frac{Z_{dp}}{K_{DP}\lambda}\right). \tag{18b}$$

Again, using the ratio of Z_{dp}/K_{DP} in this retrieval cancels out the effects of orientation and shape. Another relation for N_t included in our accuracy assessment is given by Carlin et al. (2021):

$$\log_{10}\left(N_t(Z_H, IWC)\right) = 6.69 + 2\log_{10}(IWC) - 0.1 Z_H. \tag{19}$$

Combined with IWC_{Carlin}, Eq. (19) is hereafter referred to as $N_t(Z_H, IWC_{Carlin})$. Note that polarimetric retrieval equations (Eqs. 9, 10, and 15–18a) were derived in the Rayleigh approximation assuming that the density ρ_s of Rayleigh scatterers (ice particles, snowflakes) is inversely proportional to D, according to the formula following Brandes et al. (2007):

$$\rho_s(D) = \alpha_0 f_{rim} D^{-1} = \alpha_p D^{-1}, \tag{20}$$

where ρ_s is expressed in grams per cubic centimeter, α_0 is a constant, and the prefactor α_p varies with the degree of riming f_{rim}, which ranges from 1 for unrimed ice to 5 for heavily rimed ice. For larger non-Rayleigh scatterers like graupel or hail, these polarimetric retrieval equations are not valid (Ryzhkov et al., 2020). Reliable retrievals are only obtainable in areas where Z_{DR} and K_{DP} are not very close to zero, which represents a weakness of polarimetric retrievals. In addition, a recent study showed that polarimetric ice microphysical retrievals following Ryzhkov and Zrnić (2019) provide the best results at cold temperatures, i.e., lower than -10 to -15 °C (Murphy et al., 2020). Around this temperature interval the dendritic growth layer (DGL) is located and Z_{DR} and K_{DP} exhibit pronounced signals. For this reason, our analysis is restricted to temperatures below -10 °C. Table 2 summarizes the retrieval equations used in this study.

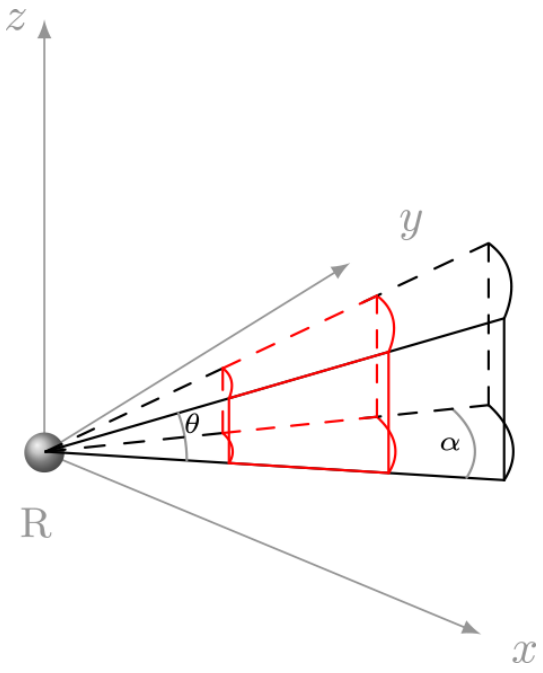

Figure 1. RSVP column (outline in red), covering an arbitrary volume in range and in azimuth.

4 Methodology

RHI scans obtain vertically high-resolved measurements and thus are well suited for microphysical studies and our accuracy assessment. Furthermore, the sequences of successive RHIs performed during the OLYMPEX campaign in azimuthal sectors of 22° provide high-resolution 3D measurements in this predefined region. Our newly introduced RHI sector vertical profile (RSVP) technique provides noise-reduced quasi-vertical profiles of polarimetric variables obtained by azimuthal averaging of RHI sector scans in a convenient height vs. time format. This method was inspired by both the quasi-vertical profile (QVP; Ryzhkov et al., 2016) methodology and the ability of CVPs to follow flight segments of research aircraft, and on top it takes advantage of the RHI scan mode. Figure 1 illustrates the RSVP technique introduced here for the matching with airborne in situ measurements.

To create a RSVP, a series of RHIs is first averaged within the azimuthal range α. The range of elevation angles θ considered can be adapted, e.g., to minimize ground clutter effects.

In the second step, windows of the desired size and position are selected along the range axis of the already azimuthally averaged RHI (marked in red in Fig. 1) and averaged along the chosen range interval as well. Based on the selected and averaged volume, a mean profile is computed representing the vertical columns that are combined and displayed in the RSVP. In this way, RSVPs enable both the

Table 2. Table of retrieval equations used in this work (D_m is in units of mm, IWC is in units of $g\,m^{-3}$, and N_t is in units of L^{-1}; T is in units of °C.)

Retrieval	Formula	Type	Reference
$D_m^{I}(Z_h)$	$1.45 {Z_h}^{0.25}$	Empirical	Skofronick-Jackson et al. (2019)
$D_m^{II}(Z_h)$	$1.06 {Z_h}^{0.271}$	Empirical	Matrosov et al. (2019)
$D_m(Z_{dp}, K_{DP})$	$-0.1 + 2.0(\frac{Z_{dp}}{K_{DP}\lambda})^{1/2}$	Empirical	Ryzhkov and Zrnić (2019)
$D_m(Z_h, K_{DP})$	$0.67(\frac{Z_h}{K_{DP}\lambda})^{1/3}$	Empirical	Bukovčić et al. (2020)
$\log_{10}(\mathrm{IWC}^{I}(Z_H, T))$	$0.06 Z_H - 0.0197 T - 1.7$	Empirical	Hogan et al. (2006)
$\log_{10}(\mathrm{IWC}^{II}(Z_H, T))$	$0.06 Z_H - 0.0212 T - 1.92$	Model	Hogan et al. (2006)
$\mathrm{IWC}(K_{DP})$	$0.903 K_{DP} + 0.319$	Empirical	Nguyen et al. (2019)
$\mathrm{IWC}^{I}(Z_{dr}, K_{DP})$	$(0.136 K_{DP} + 0.037)(\frac{1}{1 - Z_{dr}^{-1}})$	Empirical	Nguyen et al. (2019)
$\mathrm{IWC}^{II}(Z_{dr}, K_{DP})$	$4 \times 10^{-3}(\frac{K_{DP}\lambda}{1 - Z_{dr}^{-1}})$	Theoretical	Ryzhkov and Zrnić (2019)
$\mathrm{IWC}(Z_h, K_{DP})$	$0.31 {K_{DP}}^{0.66} {Z_h}^{0.28}$	Empirical	Bukovčić et al. (2020)
IWC_{Carlin}	$\begin{cases} \mathrm{IWC}^{II}(Z_{dr}, K_{DP}) \text{ if } Z_{DR} > 0.4\,\mathrm{dB}, \\ \mathrm{IWC}(Z_h, K_{DP}) \text{ otherwise} \end{cases}$	Theoretical and empirical	Carlin et al. (2021)
$\log_{10}(N_t(Z_H, Z_{dp}, K_{DP}))$	$0.1 Z_H - 2\log_{10}\gamma - 1.33$	Theoretical	Ryzhkov and Zrnić (2019)
$\log_{10}(N_t(Z_H, \mathrm{IWC}))$	$6.69 + 2\log_{10}(\mathrm{IWC}) - 0.1 Z_H$	Theoretical and empirical	Carlin et al. (2021)

joint analysis with fixed ground-based measurements provided by vertically pointing devices like, e.g., micro rain radars (MRRs) and the tracking of research aircraft within the sector covered by the RHIs for the matching with airborne measurements. In the latter case, the selected volume taken into account in the averaging process changes with time. Additionally, vertical averaging is applied, with 75 m bins to match the aircraft track and account for aircraft altitude fluctuations. Four columns with a length on the range axis of 4.5 km each starting at 2 km distance from the radar are used for tracking the aircraft. The first 2 km were omitted because of known inconsistencies in the transmitters and reduced polarimetric information content. Also, the maximum range considered in this analysis was 20 km from the radar in order to reduce partial beam blockage by surrounding mountains. The temporal resolution of the RSVP technique depends for sure on the scan schedule. During the OLYMPEX campaign, the 22 RHIs measured in the azimuthal sector were available every 4 min interspersed with a 2 min PPI scan after each two RHI sector scans.

Figure 2 shows as an example RSVPs of Z_H, Z_{DR}, ρ_{hv}, and K_{DP} for a complex occluded front observed on 18 December 2015. Similar RSVPs have been generated for all 20 flights during OLYMPEX totalling approximately 60 flight hours (not shown here). The event displayed in Fig. 2 exhibits throughout clearly visible ML signatures in Z_H, Z_{DR}, and ρ_{HV}, roughly following the temporal evolution of the 0 °C isotherm. Within the DGL, located at temperatures between −10 and −15 °C, also bands of enhanced Z_{DR} and K_{DP} are visible.

For the accuracy assessment, the microphysical retrievals introduced in Sect. 3 are calculated based on the RSVPs and displayed in a similar manner, considering only data above the ML. For this purpose, only radar data with $Z_{DR} > 0.1$ dB, $Z_H > 0$ dBZ, $K_{DP} > 0.01°\,km^{-1}$, and $\rho_{hv} > 0.7$ are used.

A direct comparison of airborne in situ measurements with ground-based retrievals requires a careful matching in both space and time. Research aircraft measure along flight trajectories, while the RSVP technique uses stationary ground-based radars monitoring a volume at flight altitude. The aircraft measurements of IWC, D_m, and N_t are averaged along the respective flight path sections and compared to the radar retrievals in the according columns and at the corresponding aircraft altitude. Similarly, the flight altitude and measured environmental parameters (e.g., temperature) are averaged for the time intervals within each column. The temperature information enables us to exclude bright band effects. Herein, the averaged in situ observations are assumed to be characteristic of the entire collocated radar volume. Figure 3 illustrates the matching of microphysical retrievals based on RSVP data with airborne in situ measurements. During OLYMPEX, the UND Citation II research aircraft performed 148 transects over DOW at different altitudes. In our study, only the aircraft measurements between 3 and 7 km height

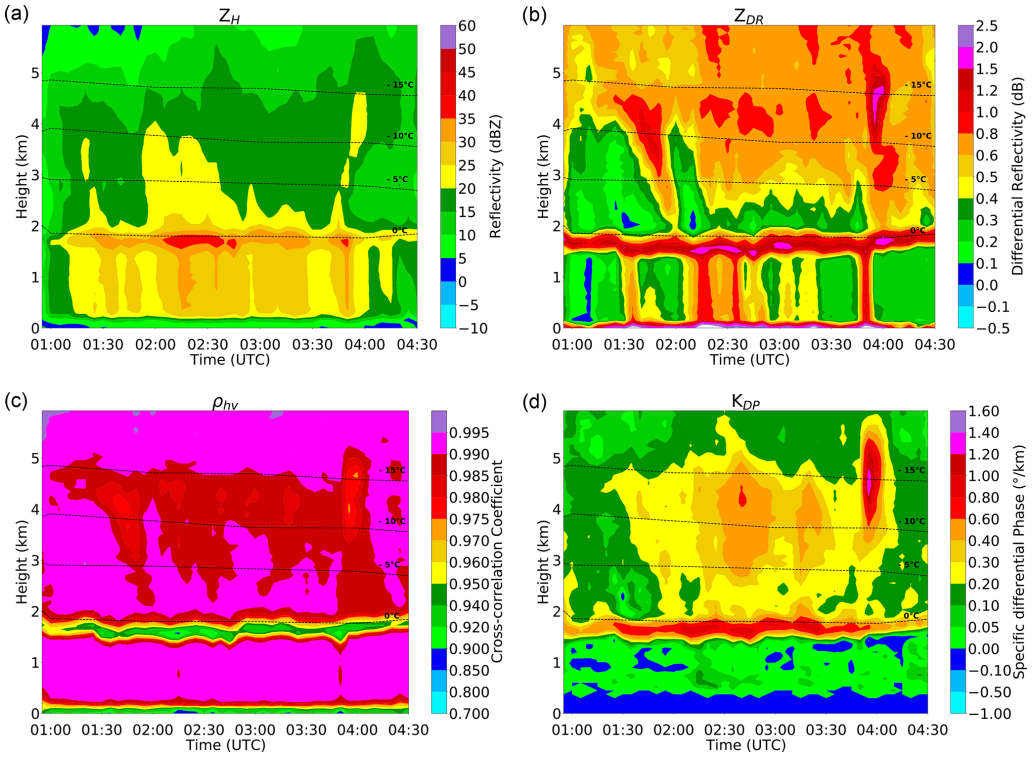

Figure 2. RSVPs of Z_H **(a)**, Z_{DR} **(b)**, ρ_{hv} **(c)**, and K_{DP} **(d)** using measurements from the DOW on 18 December 2015 between 00:40 and 04:30 UTC. The time interval shown is equal to the flight mission length to the nearest 15 min. Data in the RSVPs are at ranges from 6.5 to 11 km away from the radar and 22° in azimuth. The overlaid dashed lines (in all panels) display the 0, −5, −10, and −15 °C isotherms from European Centre for Medium-Range Weather Forecasts Reanalysis v5 (ERA5; Hersbach et al., 2020) at the DOW location.

are used. The use of RSVP columns allows for the analysis of multiple collocated data points within a single overpass. Here, the selected length of 4.5 km along the range for the RSVP columns ensures that the duration of an aircraft flying at approximately 100 m s^{-1} is sufficiently long within the column ($t \geq 30$ s). Flight intercepts of less than 30 s in duration were discarded from the analysis as they may not adequately represent the respective RSVP columns and to ensure statistical reliability. Too short flight intercepts occurred, e.g., when the aircraft shortly flew along the edge of a column and then left the sector again (e.g., yellow column in right panel of Fig. 3) or did not pass the RHI sector at all. Note that the limited temporal resolution of RSVPs (here 4 min) and the comparatively short flight segments can lead to a temporal mismatch between the two datasets of up to 3 min in this study.

5 Accuracy assessment of the ice microphysical retrievals

This section presents the resulting accuracies for all polarimetric and non-polarimetric retrievals outlined in Sect. 3 exploiting the collocated in situ measurements available during the OLYMPEX campaign. The in situ measurements are assumed to be the truth in this study despite similar existing uncertainties, e.g., with the assumed mass–dimension relationship. As statistical measures for the agreement between the in situ measurements and the different radar-derived retrievals, the mean and median retrieved-to-measured ratio (RMR), the mean difference (bias), the root mean square error (RMSE), and Pearson's correlation coefficient r are considered. Results for all ice microphysical retrievals introduced in Sect. 3 are shown in Table 3. The retrieval analysis identifies in terms of RMSE $\mathrm{IWC_{Carlin}}$, $N_t(Z_H, \mathrm{IWC_{Carlin}})$, and $D_m(Z_{dp}, K_{DP})$ as the best-performing set for the three quantities considered. It can be seen that the use of polarimetry clearly improves the estimates of IWC and D_m compared to the conventional, non-polarimetric retrievals. In particular, $\mathrm{IWC_{Carlin}}$ can improve r by 7 % over $\mathrm{IWC^I}(Z_H, T)$ and reduce RMSE by 37 %. An even greater improvement occurs for the estimation of D_m, where the use of $D_m(Z_{dp}, K_{DP})$ over both non-polarimetric D_m retrievals increases r by 15 % compared to both non-polarimetric D_m retrievals. $D_m(Z_{dp}, K_{DP})$ also brings a reduction in RMSE of 47 % compared to $D_m^I(Z_h)$. An analysis of $\mathrm{IWC^I}(Z_{dr}, K_{DP})$ in the ice regions of tropical clouds during seven flights of the HAIC-HIWC field campaign in Cayenne, French Guiana, showed an overall correlation between in situ and estimated IWCs of 0.72 and a mean RMSE of 0.52 g m^{-3} (Nguyen et al., 2019). In our

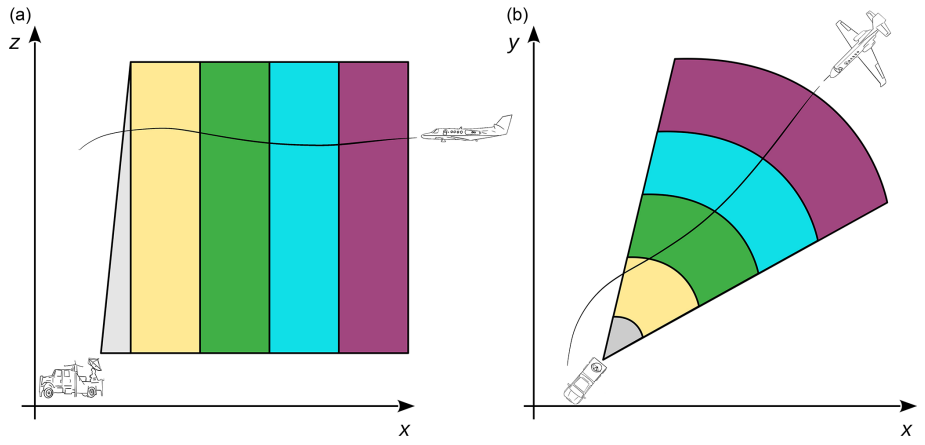

Figure 3. A schematic illustration from the collocation of RSVP columns with in situ measurements. Each colored column can be created according to the RSVP procedure depicted in Fig. 1. Gray shaded areas represent omitted data very close to the radar. Panel **(a)** shows the side view and panel **(b)** the top view of the aircraft flying through the columns.

case, a lower RMSE of 0.26 g m^{-3} can be observed for their IWC$^{\mathrm{I}}(Z_{\mathrm{dr}}, K_{\mathrm{DP}})$ and a systematically higher correlation of 0.97. Again, the advantages of using polarimetry over non-polarimetry are evident in this retrieval. It is interesting that IWC(K_{DP}) shows the highest correlation with 0.98, although Z_{dr} is not included. Nevertheless, both polarimetric estimators based on optimal fitting parameters exhibit a higher RMSE compared to all other polarimetric IWC retrievals, manifested in a systematic overestimation. A possible explanation for the overestimation may be that they were optimized for the tropical climate region characterized by an average higher IWC.

For a more detailed look at the evaluation procedure to obtain information about quantitative statistics and accuracies, we consider an example (Fig. 4) for the best-performing IWC retrieval. Out of 20 campaign flights, 10 flight missions were selected and are listed in Table 4 that have good data quality (in situ and radar) and meet all filter criteria. With the thresholds applied, the correlation of IWC$_{\mathrm{Carlin}}$ improves from $r = 0.91$ to $r = 0.96$. The slope of the filtered regression is 1.03, which is closer to the 1 to 1 line than the unfiltered green regression line. The important information here is that the filtering via thresholds provides us with a more reliable database for the analysis.

The repeated analysis without a temperature threshold applied showed a significant decrease in the correlations for all retrievals (not shown). Figure 5 shows this best-performing set of ice microphysical retrievals, together with the in situ data. Overall, we see a tendency towards a slight overestimation of IWC at warmer ($T \gtrapprox -14\,^{\circ}$C) and an underestimation at colder temperatures ($T \lessapprox -27\,^{\circ}$C), with the largest in situ standard deviation at colder temperatures. IWC$_{\mathrm{Carlin}}$ yields a high correlation of $r = 0.96$, the lowest RMSE of 0.19 g m^{-3}, and a near-zero bias of -0.04 g m^{-3}. Carlin et al. (2021) found some evidence that using IWC$_{\mathrm{Carlin}}$ for the initialization of a 1D spectral bin model results in a more constrained forecast with respect to the snowfall start time compared to using the IWC(Z_{H}, K_{DP}) retrieval only. The outstanding performance of IWC$_{\mathrm{Carlin}}$ within this accuracy assessment is in line with these findings.

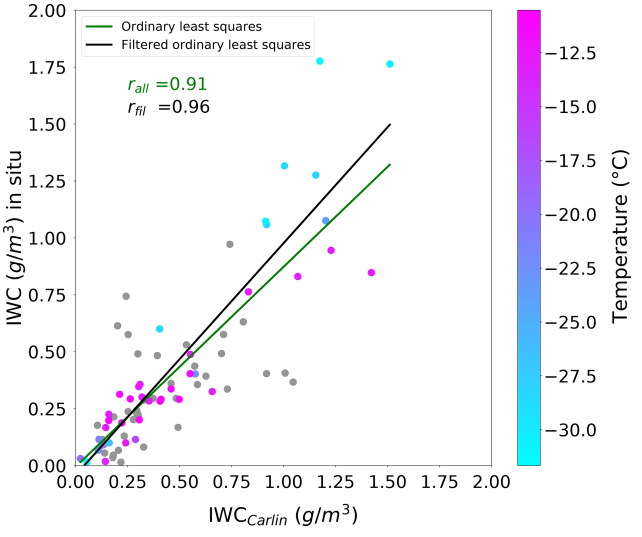

Figure 4. Scatter plots and linear regressions of IWC from OLYMPEX in situ data vs. IWC$_{\mathrm{Carlin}}$. Temperature-dependent coloring of each data point indicates temperatures colder than or equal to $-10\,^{\circ}$C, while the gray dots represent data masked via filter criteria for temperature ($T \geq -10\,^{\circ}$C) and intersection time ($t \leq 30$ s). The r statistics are reported in green for all data points and in black for filtered ones.

The polarimetric retrieval for $N_{\mathrm{t}}(Z_{\mathrm{H}}, \mathrm{IWC}_{\mathrm{Carlin}})$ poses a greater challenge (Fig. 5, middle panel). It shows a high variability and more pronounced deviations from the in situ measurements but still reaches a convincing correlation of $r = 0.91$. Similar to IWC$_{\mathrm{Carlin}}$, $N_{\mathrm{t}}(Z_{\mathrm{H}}$,IWC$_{\mathrm{Carlin}})$ shows an

Table 3. Correlations (r), slopes, and intercepts from least-squares fits, root mean square error (RMSE), biases, and mean and median retrieved-to-measured ratio (RMR) for each microphysical property and for all retrievals. Best values of each statistical measure across every microphysical retrieval type are highlighted in boldface font.

IWC ($\mathrm{g\,m^{-3}}$)	r	Slope	Intercept	RMSE	Bias	RMR mean	RMR median	Publication
$\mathrm{IWC^{I}}(Z_\mathrm{H}, T)$	0.90	0.88	−0.04	0.30	−0.11	1.23	1.59	Hogan et al. (2006)
$\mathrm{IWC^{II}}(Z_\mathrm{H}, T)$	0.91	1.40	−0.05	0.30	0.10	0.79	**1.00**	Met Office Model
$\mathrm{IWC_{Comb}}(Z_\mathrm{H}, T)$	0.95	1.18	−0.06	0.20	**0.02**	**0.95**	1.11	$\mathrm{IWC^{I}}(Z_\mathrm{H}, T)$, $\mathrm{IWC^{II}}(Z_\mathrm{H}, T)$
$\mathrm{IWC}(K_\mathrm{DP})$	**0.98**	1.29	−0.42	0.28	−0.22	1.46	2.02	Nguyen et al. (2019)
$\mathrm{IWC^{I}}(Z_\mathrm{dr}, K_\mathrm{DP})$	0.97	1.20	−0.34	0.26	−0.21	1.43	1.97	Nguyen et al. (2019)
$\mathrm{IWC^{II}}(Z_\mathrm{dr}, K_\mathrm{DP})$	0.94	0.87	**−0.02**	0.24	−0.10	1.21	1.25	Ryzhkov et al. (2018)
$\mathrm{IWC}(Z_\mathrm{H}, K_\mathrm{DP})$	0.94	**1.00**	−0.10	0.23	−0.10	1.22	1.76	Bukovčić et al. (2018)
$\mathrm{IWC_{Carlin}}$	0.96	1.03	−0.05	**0.19**	−0.04	1.08	1.13	Carlin et al. (2021)
$N_\mathrm{t}\log_{10}\,(\mathrm{L^{-}1})$								
$N_t(Z_\mathrm{H}, Z_\mathrm{dp}, K_\mathrm{DP})$	0.88	**1.13**	**−0.33**	0.46	−0.18	1.17	1.33	Ryzhkov et al. (2018)
$N_t(Z_\mathrm{H}, \mathrm{IWC_{Carlin}})$	**0.91**	1.38	−0.52	**0.43**	**−0.09**	**1.08**	**1.27**	Carlin et al. (2021)
D_m (mm)								
$D_\mathrm{m}^{\mathrm{I}}(Z_\mathrm{h})$	0.79	0.55	0.04	2.12	−1.82	1.78	1.86	Skofronick-Jackson et al. (2019)
$D_\mathrm{m}^{\mathrm{II}}(Z_\mathrm{h})$	0.79	**0.64**	0.19	1.40	−0.99	1.42	1.48	Matrosov et al. (2019)
$D_\mathrm{m}(Z_\mathrm{h}, K_\mathrm{DP})$	**0.94**	2.60	−0.85	1.38	1.10	0.53	0.54	Bukovčić et al. (2018)
$D_\mathrm{m}(Z_\mathrm{dp}, K_\mathrm{DP})$	0.91	1.59	**0.01**	**1.13**	**0.87**	**0.63**	**0.74**	Ryzhkov et al. (2018)

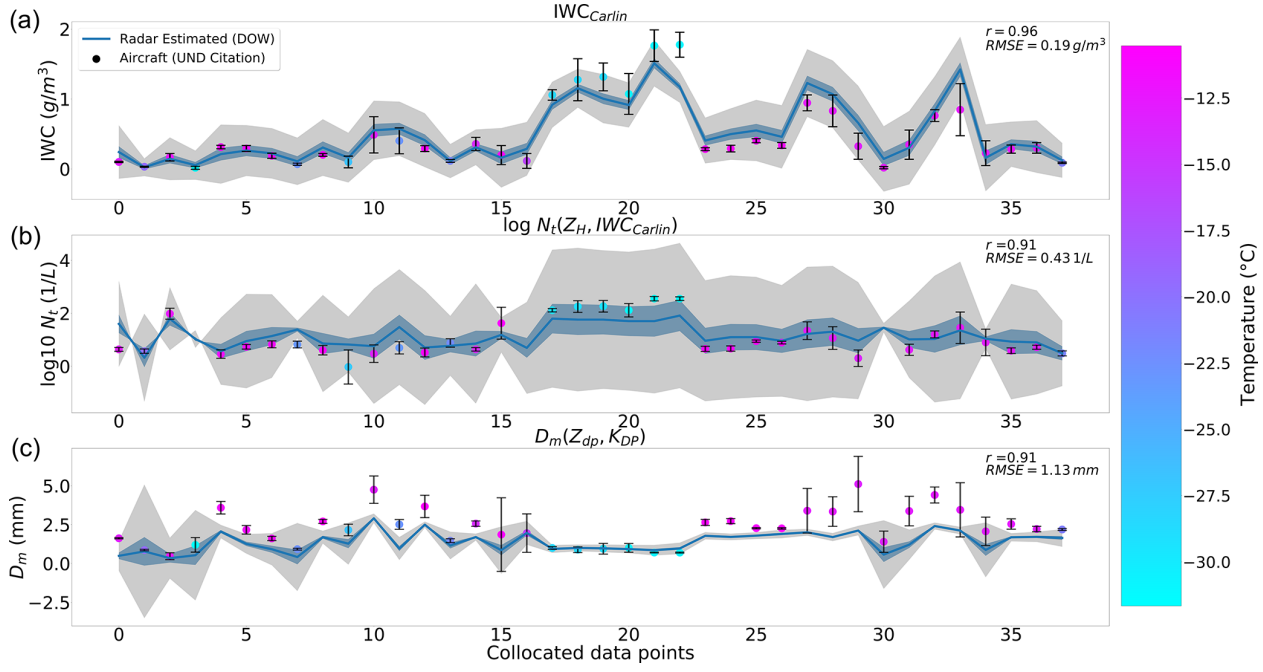

Figure 5. Collocated aircraft in situ data in chronological order (colored dots) and the best-performing set of ice microphysical retrievals based on RSVP data (solid blue lines) for 10 flight missions. Plots represent from top to bottom $\mathrm{IWC_{Carlin}}$, $N_\mathrm{t}(Z_\mathrm{H}, \mathrm{IWC_{Carlin}})$, and $D_\mathrm{m}(Z_\mathrm{dp}, K_\mathrm{DP})$. Shadings show $\pm 1\sigma$ (gray) and standard error of the mean (blue) calculated via Gaussian error propagation. Colors following the color bar indicate the respective temperatures (in °C). Vertical bars represent in situ standard deviations.

Table 4. List of selected Citation II flight missions after applying filter criteria with resulting collocated data points.

Dates	Flight times (UTC; to nearest 15 min)	Data points
12 November	19:30–22:30	0–1
13 November	15:00–17:45	2–3
1 December	22:45–01:45	4–8
4 December	13:00–16:00	9–11
5 December	14:45–18:00	12–14
10 December	14:45–17:00	15–22
12 December	17:00–20:15	23–26
13 December	15:45–19:15, 20:00–23:15	27–34
18 December	01:15–04:30	35–37

overestimation at warmer ($T \gtrapprox -14\,^{\circ}\mathrm{C}$) and underestimation at colder temperatures ($T \lessapprox -27\,^{\circ}\mathrm{C}$). Pronounced N_t deviations at warmer temperatures are visible for the collocated data points 29 and 31, with the former also revealing large standard deviations on the in situ side. The outlier at data point 9 exhibits K_DP values below $0.1\,^{\circ}\,\mathrm{km}^{-1}$, which may indicate deficiencies of this retrieval for very low K_DP values, but the in situ values show relatively high variability as well. The $D_\mathrm{m}(Z_\mathrm{dp}, K_\mathrm{DP})$ retrieval (Fig. 5, bottom panel) estimates particle size especially well at colder temperatures. Mixtures of aggregates with different sizes coexisting near the ML (solid region) may explain the high in situ standard deviations at warmer temperatures (e.g., data point 29 where D_m is in excess of 5 mm). Furthermore, the occurrence of an increased number of aggregates reducing the information content of K_DP can result in an underestimation of $D_\mathrm{m}(Z_\mathrm{dp}, K_\mathrm{DP})$, which makes D_m estimation via polarimetric retrievals close to the freezing level challenging. In line with our analyses, Murphy et al. (2020) indicated larger errors with polarimetric N_t and D_m retrievals in the immediate vicinity of the ML. Despite this underestimation, a convincing correlation of $r = 0.91$ is obtained.

Direct comparisons of both $\mathrm{IWC}(Z, T)$ retrievals with the $\mathrm{IWC_{Carlin}}$ retrieval reveals that both non-polarimetric retrievals show a worse performance in terms of lower correlation and higher RMSE (see Table 3). Note that the use of temperature information from soundings or models would further reduce the performance of $\mathrm{IWC}(Z, T)$ retrievals due to increased uncertainties compared to in situ temperature data recorded during the flights. Figure 6 indicates that each $\mathrm{IWC}(Z, T)$ shows a better performance in a certain temperature range. Accordingly, we combined them using Eq. (11) for $T \leq 15\,^{\circ}\mathrm{C}$ and Eq. (12) elsewhere; i.e., the DGL located between approximately -10 to $-15\,^{\circ}\mathrm{C}$ providing the optimal conditions for the depositional growth of ice serves here as the boundary for the two retrievals. This combination, hereafter referred to as $\mathrm{IWC_{Comb}}(Z_\mathrm{H}, T)$, shows promise in estimating IWC with non-polarimetric data more precisely, as it reduces the RMSE to 0.20 and increases the correlation to 0.95 (Table 3). The bias of the combined method with a value of $0.02\,\mathrm{g\,m}^{-3}$ is slightly closer to 0 compared to $\mathrm{IWC_{Carlin}}$. However, a more extensive dataset is needed to corroborate this finding.

Heymsfield et al. (2008) also evaluated non-polarimetric IWC retrieval methods, including the $\mathrm{IWC^I}(Z_\mathrm{H}, T)$ variant for 95 GHz, using test datasets derived from in situ microphysical measurements. The retrieved-to-measured ratio (RMR) was calculated via dividing the mean or median of the retrieved quantity by the measured quantity, with a selected range of $0.75 < \mathrm{RMR} < 1.25$ indicating "good" agreement between retrievals and measurements. Their $\mathrm{IWC^I}(Z_\mathrm{H}, T)$ showed a tendency to underestimate IWC at low temperatures and overestimate it at warm temperatures, consistent with our results. Overall, their non-polarimetric radar-only approach and radar temperature retrievals yielded a mean (median) RMR of 1.29 (1.20). Our analysis shows a similar mean RMR of 1.23 for $\mathrm{IWC^I}(Z_\mathrm{H}, T)$ but a slightly higher median RMR value of 1.59. It is noteworthy that the polarimetric $\mathrm{IWC_{Carlin}}$ outperforms $\mathrm{IWC^I}(Z_\mathrm{H}, T)$ and their radar-only and radar temperature retrievals, with a mean RMR close to unity (see Table 3).

Figure 7 also demonstrates the pronounced biases associated with the $D_\mathrm{m}^\mathrm{I}(Z_\mathrm{h})$ and $D_\mathrm{m}^\mathrm{II}(Z_\mathrm{h})$ retrievals, with especially large deviations (strong overestimation) at colder temperatures. This result underlines again the importance of the key variable K_DP in ice and reveals the notorious inaccuracies of conventional D_m retrievals. However, these power laws could potentially be used in combination with polarimetric D_m retrieval in areas near the ML in a hybrid fashion to obtain a more accurate estimate of D_m.

Our analysis of $N_\mathrm{t}(Z_\mathrm{H}, \mathrm{IWC_{Carlin}})$ shows good agreement in terms of mean RMR (1.08), whereas none of the D_m retrievals in this evaluation fall within the chosen RMR range, with the best-performing $D_\mathrm{m}(Z_\mathrm{dp}, K_\mathrm{DP})$ exhibiting a RMR median value close to the lower limit with a value of 0.74. Overall, our analysis is consistent with findings by Murphy et al. (2020), who found a strong underestimation of the $D_\mathrm{m}(Z_\mathrm{dp}, K_\mathrm{DP})$ retrieval near the ML. Similarly, our analysis shows the best results in regions with high Z_DR and K_DP, such as in the DGL, and the worst just above the freezing level, where Z_DR and K_DP signatures nearly vanish as a result of aggregation processes (Ryzhkov et al., 1998).

6 Discrepancy analyses

For a more detailed analysis and improved understanding, examples of the most pronounced discrepancies encountered between in situ and retrieved quantities are spotlighted and presented, together with CPI imagery, HVPS samples, and/or RSVPs.

On 10 December 2015 at 15:58 UTC (data point 22, see top panel in Fig. 5), the aircraft entered the RSVP column at a distance of 15.5 to 20 km from the DOW. In this flight seg-

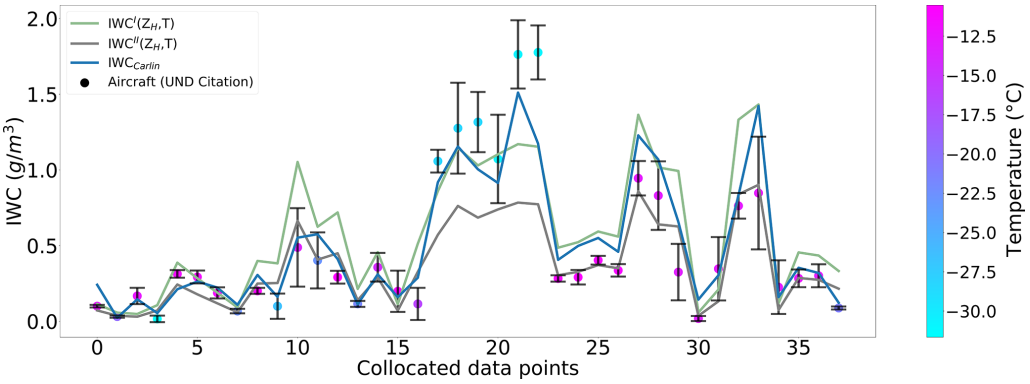

Figure 6. Collocated aircraft in situ data in chronological order (colored dots), the $\mathrm{IWC}^{\mathrm{I}}(Z_{\mathrm{H}}, T)$ (green), the $\mathrm{IWC}^{\mathrm{II}}(Z_{\mathrm{H}}, T)$ (gray), and the $\mathrm{IWC}_{\mathrm{Carlin}}$ (blue) of RSVP data (solid lines) for 10 flight missions. Vertical bars have the same meaning as in Fig. 5.

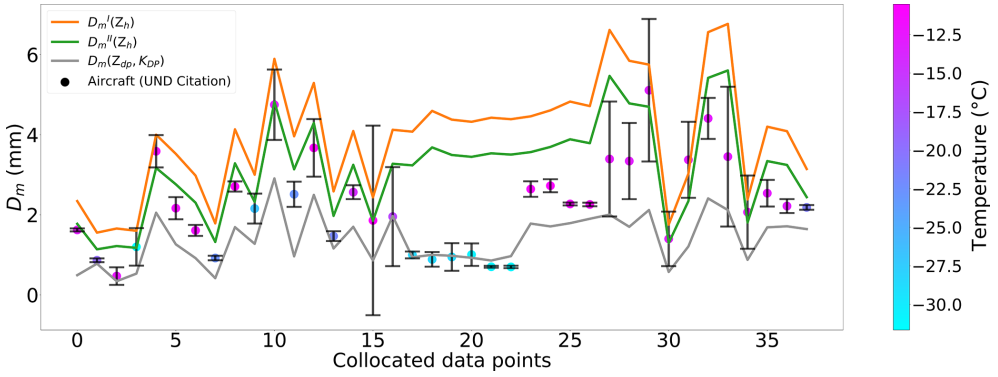

Figure 7. Collocated aircraft in situ data in chronological order (colored dots), the D_{m} power laws (yellow and green), and the $D_{\mathrm{m}}(Z_{\mathrm{dp}}, K_{\mathrm{DP}})$ retrieval (gray) of RSVP data (solid lines) for 10 flight missions. Vertical bars have the same meaning as in Fig. 5.

ment, a mean temperature of −31 °C was measured by the Citation II at a mean altitude of 5.7 km. The discrepancy between in situ observed IWC and retrieved $\mathrm{IWC}_{\mathrm{Carlin}}$ is striking here, with an underestimation of 0.61 g m^{-3} by the radar-based retrieval. This is the only data point where the IWC discrepancy is so pronounced that even the uncertainty estimates via the standard deviations from both in situ and retrieval side do not show any overlap. One possible reason for the underestimation by $\mathrm{IWC}_{\mathrm{Carlin}}$ is the temporal mismatch displayed in Fig. 8. Since the aircraft entered at 15:58 UTC and left at 15:59 UTC, the collocation was assigned to the RHI sector scan that began at 15:54 UTC. Thus, it is temporally at the very end of this sector scan. However, the subsequent one might contain signatures that had already been started to be measured at the end of the previous sector scan. For instance, a higher IWC due to advection at the end of the scan could be present. Note that two RHI sector scans are always followed by a PPI scan of 2 min. The following RHI sector scan starting at 16:00 UTC is also close in time to the in situ measurements and shows a higher IWC of 1.39 g m^{-3}, reducing the discrepancy to 0.39 g m^{-3}. Moreover, choosing this scan leads to overlapping standard deviations, with a retrieval σ of 0.45 g m^{-3}. However, this data point also shows the slight underestimation of $\mathrm{IWC}_{\mathrm{Carlin}}$ at colder temperatures.

The most pronounced discrepancy in terms of D_{m} emerges on 13 December 2015 at 16:17 UTC (data point 29, see lower panel in Fig. 5) when the aircraft entered the RSVP column at a distance of 6.5 to 11 km from the DOW. Here, the Citation II measured a mean temperature of −13 °C at a mean altitude of 2.95 km. Retrieved $D_{\mathrm{m}}(Z_{\mathrm{dp}}, K_{\mathrm{DP}})$ strongly underestimates the in situ observed D_{m} peak exceeding 5 mm, with an underestimation of almost 3 mm. Note that in this case there is no temporal mismatch. Figure 9 illustrates sampled particles captured along the relatively narrow flight path of the aircraft. It seems the smaller in situ sample is dominated by larger particles, while the larger RSVP volume also accounts for the immediate vicinity where more smaller particles may be present. These possibly affect $D_{\mathrm{m}}(Z_{\mathrm{dp}}, K_{\mathrm{DP}})$ significantly due to averaging and may not properly resolve the regions with enhanced in situ D_{m} peaks. In addition, the DOW sector scan started at 16:14 UTC, and thus the RSVP volume also contains particles not monitored by the aircraft entering the sector later. The particles may be smaller and could explain the discrepancy between in situ observed D_{m} and retrieved $D_{\mathrm{m}}(Z_{\mathrm{dp}}, K_{\mathrm{DP}})$. It is also worth mentioning that

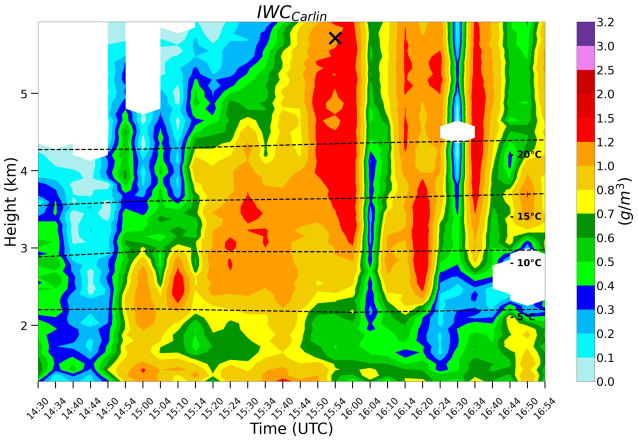

Figure 8. RSVPs of IWC_{Carlin} at ranges between 15.5 and 20 km from the DOW on 10 December 2015 between 14:30 and 16:54 UTC. Overlaid dashed lines display the −5, −10, −15, and −20 °C isotherms from ERA5 at the DOW location. The collocated data point is indicated by the black cross.

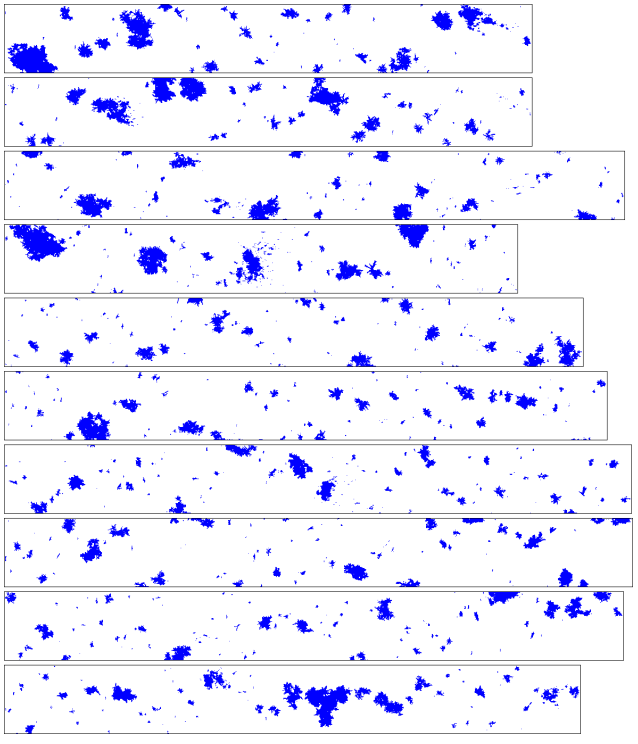

Figure 9. HVPS sample images of hydrometeor shadows on 13 December 2015 at 16:18 UTC. The images correspond to the trajectory within the DOW sector scan starting at 16:17 UTC. The height of each panel represents 19.2 mm.

an in situ σ of 1.78 mm is observed along the trajectory, indicating high variability in this region.

In agreement with the RICE measurements, indicating the presence of SLW with a sudden decrease in frequency (Fig. 10), the CPI example particle images in Fig. 11 also in-

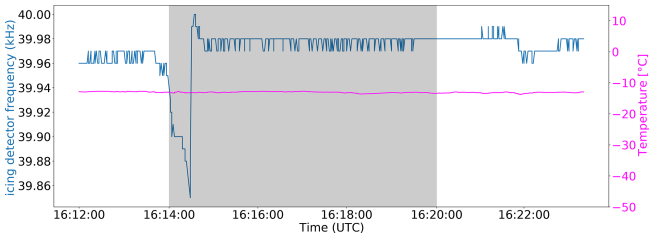

Figure 10. RICE oscillation frequency (blue) and temperature at Citation II level (magenta). Icing periods are indicated by a sharp drop in RICE frequency due to ice accumulation at the sensor tip. The shaded area represents the associated flight interval on 13 December 2015.

dicate ongoing riming in the flight segment under discussion. Moreover, a clear sagging of the ML in terms of Z_{DR} and ρ_{hv} (not shown) in the RSVPs supports the riming hypothesis, since rimed ice particles fall with increased velocities and therefore melt at lower altitudes. Such a sagging signature in radar images can be associated with riming processes (Kumjian et al., 2016), and since riming, most likely present in this case, results in both higher φ and f_{rim} values than assumed in the derivation of the $D_m(Z_{dp}, K_{DP})$ retrieval, the observed underestimation is in line with the known shortcomings of the retrieval for such conditions. Additionally, for riming conditions present, the mass–dimension relation assumed for in situ measured IWC is also not valid anymore. In general, the precise effect of riming on mass–dimension relations is poorly understood (Tridon et al., 2019), but these processes considerably modify inherent parameters. With an increasing degree of riming, higher values of the prefactor a and the exponent b in Eq. (6) are expected. The latter can reach a maximum b close to 3 (sphere-like geometry) when graupel-like particles filled with rime are present. Thus, the observed overestimation of IWC_{Carlin} could at least partly be explained by assumed inappropriate parameters in the mass–dimension relationship following Brown and Francis (1995). Using a relation that accounts for more knowledge of ice particle masses (e.g., Heymsfield et al., 2010) that is valid for higher degrees of riming (e.g., Leinonen and Szyrmer, 2015) or that uses multiple mass–dimension relations for different D_{mm} ranges, as proposed in Ding et al. (2020), may reduce deviations between in situ and retrieved IWC in this case. Only directly measured in situ IWC can provide IWC without the need for any assumptions. However, such measurements were not available during the OLYMPEX campaign (Tridon et al., 2019).

7 Conclusions

Data collected during the OLYMPEX campaign (Houze et al., 2017) conducted in late 2015 provided a comprehensive database including ground-based polarimetric X-band radar measurements and airborne in situ cloud measure-

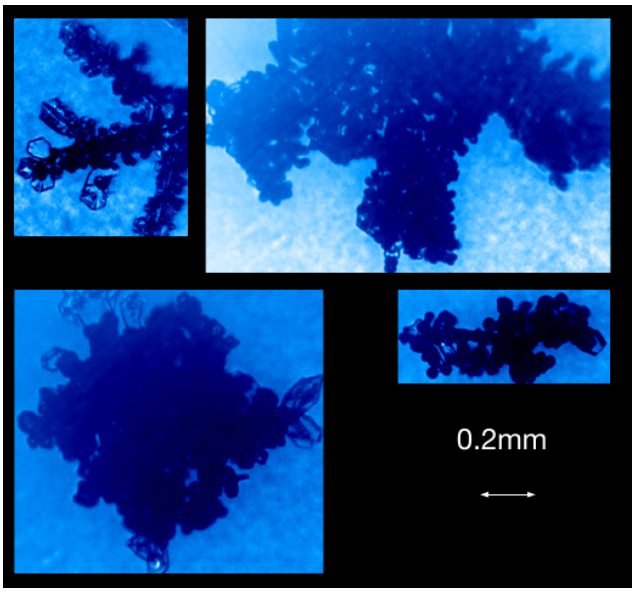

Figure 11. Examples of CPI images where rimed crystals were observed. The images were taken on 13 December 2015 between 16:14 and 16:18 UTC.

ments to evaluate radar-based ice microphysical retrievals. In this study, the accuracy of conventional non-polarimetric retrievals is assessed, together with a series of state-of-the-art polarimetric retrievals to quantify the benefits of additional polarimetric information and identify the strengths and weaknesses of all of them. RHIs within an azimuthal sector of 22° provide vertically high-resolved polarimetric measurements, and the RSVP matching methodology introduced adds a moderate degree of averaging in order to reduce the noisiness of especially phase-based radar measurements like K_{DP}. The matching of the achieved robust radar-based retrievals with the airborne cloud measurements enables the accuracy assessment of retrievals for ice water content (IWC), ice particle number concentration N_t, and mean volume diameter D_m, which are of great value for model evaluation and data assimilation. The key results of the study are as follows.

1. State-of-the-art microphysical retrievals exploiting polarimetric radar measurements to estimate IWC (RMSE $= 0.19\,g\,m^{-3}$), N_t (RMSE $= 0.43\,L^{-1}$), and D_m (RMSE $= 1.13$ mm) achieve quite high agreement with airborne in situ measurements, especially at cold temperatures.

2. Overall, polarimetric retrievals are superior to conventional Z-based retrievals, but combinations with non-polarimetric retrievals have potential to improve deficiencies directly above the ML.

3. The hybrid polarimetric IWC_{Carlin} retrieval outperforms all other IWC estimates in terms of RMSE and shows a high r of 0.96.

4. Compared to IWC retrievals, the N_t and D_m retrievals show larger uncertainties and should be further improved in the future.

This study clearly demonstrates the added value of multiparameter retrievals as proposed by Carlin et al. (2021) for the IWC. Combining the strengths of retrievals can be applied to other ice microphysical properties and ultimately also hints at the potential for developing combinations of polarimetric and non-polarimetric retrievals. Further independent evaluation studies particularly focusing on such hybrid retrievals are required.

Future work using an additional particle classifier (e.g., Praz et al., 2018; Przybylo et al., 2022) capable of identifying and classifying each particle along flight transects with high-resolution image data sampled by particle imagers will provide an even more in-depth evaluation. Specifically, extended classifiers that possibly allow riming degree estimation, as proposed in Przybylo et al. (2022), may provide an avenue for studying riming cases and relating these observations to retrieval assumptions. These classifiers hold the potential to be utilized for the refinement and development of future ice microphysical retrieval methods.

The exploitation of the OLYMPEX data represents another piece of the mosaic towards a comprehensive evaluation of (polarimetric) microphysical retrievals. While previous evaluation studies focused on C- and S-band radar data, this study also emphasizes the added value of X-band radars for the exploitation of microphysical retrievals and related process studies. However, in light of potential applications in model evaluation and data assimilation, C- and S-band radars are of great interest because of their national operational availability. Recently, even more field campaigns have been exploited or their analysis is currently underway. Examples are the Federal-Aviation-Administration-led In-Cloud ICing and Large-drop Experiment (ICICLE; Bernstein et al., 2021) and the NASA-led Investigation of Microphysics and Precipitation for Atlantic Coast-Threatening Snowstorms (IMPACTS; McMurdie et al., 2019). Two flight legs of a winter storm case from the latter campaign have already been used by Dunnavan et al. (2022) for a radar retrieval evaluation. With respect to previous experimental evaluation studies, the more convincing accuracy of the best-performing polarimetric retrievals identified in this study gives us further confidence in their application. The benefit of using a shorter wavelength than that of S-band radars, as suggested in Ryzhkov et al. (1998) for the verification of their proposed $IWC^I(Z_{dr}, K_{DP})$, indeed exhibited a noticeably lower RMSE in our study ($0.24\,g\,m^{-3}$ vs. $0.4\,g\,m^{-3}$). Using the same $IWC^I(Z_{dr}, K_{DP})$ retrieval as Nguyen et al. (2019), we were further able to achieve half the RMSE and a systematically higher correlation with our method based on RHI sector scans, even though both studies used an X-band radar. More recent retrievals were able to achieve even smaller RMSEs. The almost consistent underestimation of $D_m(Z_{dp}, K_{DP})$ shown in Murphy

et al. (2020) is in line with our results. However, in contrast to their study, we could not only attribute the deficits to warmer temperature regimes but also demonstrate the accurate estimation at cold temperatures. As a result, an important open question for future research concerns the deficient performance of retrievals directly above the ML and requires new approaches to obtain accurate estimators in this region.

Data availability. OLYMPEX data used in this study were obtained from the NASA EOSDIS GHRC OLYMPEX data archive (https://doi.org/10.5067/GPMGV/OLYMPEX/DATA101, Petersen et al., 2018, and https://doi.org/10.5067/GPMGV/OLYMPEX/DOW/DATA201, Houze et al., 2018). The ERA5 data are stored at the Climate Data Store from the ECMWF and are accessible via https://doi.org/10.24381/cds.bd0915c6 (Hersbach et al., 2023).

Author contributions. AB and ST jointly developed the concept and methodology for this work. Data handling and analysis were performed by AB with contributions from MM. Visualization was carried out by AB, who also led the writing with input from ST. AJH processed the Citation II data collected during OLYMPEX and provided scientific expertise on in situ data. All authors contributed to the proofreading and added valuable suggestions to the final draft.

Competing interests. The contact author has declared that none of the authors has any competing interests.

Disclaimer. Publisher's note: Copernicus Publications remains neutral with regard to jurisdictional claims in published maps and institutional affiliations.

Special issue statement. This article is part of the special issue "Fusion of radar polarimetry and numerical atmospheric modelling towards an improved understanding of cloud and precipitation processes (ACP/AMT/GMD inter-journal SI)". It is not associated with a conference.

Acknowledgements. The research was carried out in the framework of the Priority Programme SPP-2115 "Polarimetric Radar Observations meet Atmospheric Modelling (PROM)" funded by the German Research Foundation (DFG). We also thank all the participants of OLYMPEX for collecting the data used in this study. Similarly, we acknowledge the support of Kai Mühlbauer and the open-source radar library wradlib (https://docs.wradlib.org/en/stable/index.html, last access: 11 November 2022) regarding the processing of radar data.

Financial support. This research has been supported by the Deutsche Forschungsgemeinschaft (grant nos. TR 1023/13-1 and VO 1504/5-1) and the National Aeronautics and Space Administration (grant no. 80NSSC20K0897 to Andrew J. Heymsfield).

This open-access publication was funded by the University of Bonn.

Review statement. This paper was edited by Patric Seifert and reviewed by two anonymous referees.

References

Allabakash, S., Lim, S., Chandrasekar, V., Min, K., Choi, J., and Jang, B.: X-band dual-polarization radar observations of snow growth processes of a severe winter storm: Case of 12 December 2013 in South Korea, J. Atmos. Ocean. Tech., 36, 1217–1235, https://doi.org/10.1175/JTECH-D-18-0076.1, 2019.

Aydin, K. and Tang, C.: Relationships between IWC and polarimetric radar measurands at 94 and 220 GHz for hexagonal columns and plates, J. Atmos. Ocean. Tech., 14, 1055–1063, https://doi.org/10.1175/1520-0426(1997)014<1055:RBIAPR>2.0.CO;2, 1997.

Baker, B. and Lawson, R. P.: Improvement in determination of ice water content from two-dimensional particle imagery. Part I: Image-to-mass relationships, J. Appl. Meteorol. Clim., 45, 1282–1290, https://doi.org/10.1175/JAM2398.1, 2006.

Bansemer, A.: System for OAP Data Analysis, v2.23.0, Zenodo [code], https://doi.org/10.5281/zenodo.7803116, 2023.

Baumgardner, D. and Rodi, A.: Laboratory and wind tunnel evaluations of the Rosemount icing detector, J. Atmos. Ocean. Tech., 6, 971–979, https://doi.org/10.1175/1520-0426(1989)006<0971:LAWTEO>2.0.CO;2, 1989.

Baumgardner, D., Abel, S. J., Axisa, D., Cotton, R., Crosier, J., Field, P., Gurganus, C., Heymsfield, A., Korolev, A., Krämer, M., Lawson, P., McFarquhar, G., Ulanowski, Z., and Um, J.: Cloud Ice Properties: In Situ Measurement Challenges, Meteor. Mon., 58, 9.1–9.23, https://doi.org/10.1175/AMSMONOGRAPHS-D-16-0011.1, 2017.

Bernstein, B., DiVito, S., Riley, J. T., Landolt, S., Haggerty, J., Thompson, G., Adriaansen, D., Serke, D., Kessinger, C., Tessendorf, S., Wolde, M., Korolev, A., Brown, A., Nichman, L., Sims, D., Dumont, C.: The In-Cloud Icing and Large-Drop Experiment Science and Operations Plan, Tech. rep. no. DOT/FAA/TC-21/29, Department of Transportation, Federal Aviation Administration, United States, https://doi.org/10.21949/1524472, 2021.

Brandes, E. A., Ikeda, K., Zhang, G., Schönhuber, M., and Rasmussen, R. M.: A statistical and physical description of hydrometeor distributions in Colorado snowstorms using a video disdrometer, J. Appl. Meteorol. Clim., 46, 634–650, https://doi.org/10.1175/JAM2489.1, 2007.

Brown, P. R. A. and Francis, P. N.: Improved Measurements of the Ice Water Content in Cirrus Using a Total-Water Probe, J. Atmos. Ocean. Tech., 12, 410–414, https://doi.org/10.1175/1520-0426(1995)012<0410:imotiw>2.0.co;2, 1995.

Bukovčić, P., Zrnić, D., and Zhang, G.: Winter precipitation liquid–ice phase transitions revealed with polarimetric radar and 2DVD observations in central Oklahoma, J. Appl. Meteorol. Clim., 56, 1345–1363, https://doi.org/10.1175/JAMC-D-16-0239.1, 2017.

Bukovčić, P., Ryzhkov, A., Zrnić, D., and Zhang, G.: Polarimetric radar relations for quantification of snow based on disdrometer data, J. Appl. Meteorol. Clim., 57, 103–120, https://doi.org/10.1175/JAMC-D-17-0090.1, 2018.

Bukovčić, P., Ryzhkov, A., and Zrnić, D.: Polarimetric relations for snow estimation—Radar verification, J. Appl. Meteorol. Clim., 59, 991–1009, https://doi.org/10.1175/JAMC-D-19-0140.1, 2020.

Carlin, J. T., Ryzhkov, A. V., Snyder, J. C., and Khain, A.: Hydrometeor mixing ratio retrievals for storm-scale radar data assimilation: Utility of current relations and potential benefits of polarimetry, Mon. Weather Rev., 144, 2981–3001, https://doi.org/10.1175/MWR-D-15-0423.1, 2016.

Carlin, J. T., Reeves, H. D., and Ryzhkov, A. V.: Polarimetric Observations and Simulations of Sublimating Snow: Implications for Nowcasting, J. Appl. Meteorol. Clim., 60, 1035–1054, https://doi.org/10.1175/JAMC-D-21-0038.1, 2021.

Chase, R. J., Finlon, J. A., Borque, P., McFarquhar, G. M., Nesbitt, S. W., Tanelli, S., Sy, O. O., Durden, S. L., and Poellot, M. R.: Evaluation of Triple-Frequency Radar Retrieval of Snowfall Properties Using Coincident Airborne In Situ Observations During OLYMPEX, Geophys. Res. Lett., 45, 5752–5760, https://doi.org/10.1029/2018gl077997, 2018.

Davis, C., Atkins, N., Bartels, D., Bosart, L., Coniglio, M., Bryan, G., Cotton, W., Dowell, D., Jewett, B., Johns, R., Jorgensen, D., Knievel, J., Knupp, K., Lee, W.-C., McFarquhar, G., Moore, J., Przybylinski, R., Rauber, R., Smull, B., Trapp, R., Trier, S., Wakimoto, R., Weisman, M., and Ziegler, C.: The Bow Echo and MCV experiment: observations and opportunities: observations and opportunities, B. Am. Meteorol. Soc., 85, 1075–1094, https://doi.org/10.1175/BAMS-85-8-1075, 2004.

Ding, S., McFarquhar, G. M., Nesbitt, S. W., Chase, R. J., Poellot, M. R., and Wang, H.: Dependence of mass–dimensional relationships on median mass diameter, Atmosphere, 11, 756, https://doi.org/10.3390/atmos11070756, 2020.

Dunnavan, E. L., Carlin, J. T., Hu, J., Bukovčić, P., Ryzhkov, A. V., McFarquhar, G. M., Finlon, J. A., Matrosov, S. Y., and Delene, D. J.: Radar Retrieval Evaluation and Investigation of Dendritic Growth Layer Polarimetric Signatures in a Winter Storm, J. Appl. Meteorol. Clim., 61, 1685–1711, https://doi.org/10.1175/JAMC-D-21-0220.1, 2022.

Hersbach, H., Bell, B., Berrisford, P., Hirahara, S., Horányi, A., Muñoz-Sabater, J., Nicolas, J., Peubey, C., Radu, R., Schepers, D., Simmons, A., Soci, C., Abdalla, S., Abellan, X., Balsamo, G., Bechtold, P., Biavati, G., Bidlot, J., Bonavita, M., De Chiara, G., Dahlgren, P., Dee, D., Diamantakis, M., Dragani, R., Flemming, J., Forbes, R., Fuentes, M., Geer, A., Haimberger, L., Healy, S., Hogan, R. J., Hólm, E., Janisková, M., Keeley, S., Laloyaux, P., Lopez, P., Lupu, C., Radnoti, G., de Rosnay, P., Rozum, I., Vamborg, F., Villaume, S., Thépaut, J.-N.: The ERA5 global reanalysis, Q. J. Roy. Meteor. Soc., 146, 1999–2049, https://doi.org/10.1002/qj.3803, 2020.

Hersbach, H., Bell, B., Berrisford, P., Biavati, G., Horányi, A., Muñoz Sabater, J., Nicolas, J., Peubey, C., Radu, R., Rozum, I., Schepers, D., Simmons, A., Soci, C., Dee, D., and Thépaut, J.-N.: ERA5 hourly data on pressure levels from 1940 to present, Copernicus Climate Change Service (C3S) Climate Data Store (CDS) [data set], https://doi.org/10.24381/cds.bd0915c6, 2023.

Heymsfield, A., Bansemer, A., Heymsfield, G., Noone, D., Grecu, M., and Toohey, D.: Relationship of Multiwavelength Radar Measurements to Ice Microphysics from the IMPACTS Field Program, J. Appl. Meteorol. Clim., 62, 289–315, https://doi.org/10.1175/JAMC-D-22-0057.1, 2023.

Heymsfield, A. J. and Miloshevich, L. M.: Evaluation of liquid water measuring instruments in cold clouds sampled during FIRE, J. Atmos. Ocean. Tech., 6, 378–388, https://doi.org/10.1175/1520-0426(1989)006<0378:EOLWMI>2.0.CO;2, 1989.

Heymsfield, A. J., Protat, A., Bouniol, D., Austin, R. T., Hogan, R. J., Delanoë, J., Okamoto, H., Sato, K., van Zadelhoff, G.-J., Donovan, D. P., and Wang, Z.: Testing IWC retrieval methods using radar and ancillary measurements with in situ data, J. Appl. Meteorol. Clim., 47, 135–163, https://doi.org/10.1175/2007JAMC1606.1, 2008.

Heymsfield, A. J., Schmitt, C., Bansemer, A., and Twohy, C. H.: Improved representation of ice particle masses based on observations in natural clouds, J. Atmos. Sci., 67, 3303–3318, https://doi.org/10.1175/2010JAS3507.1, 2010.

Heymsfield, A. J., Bansemer, A., and Poellot, M. R.: GPM Ground Validation NCAR Particle Probes OLYMPEX, NASA EOSDIS Global Hydrology Resource Center Distributed Active Archive Center [data set], Huntsville, Alabama, U.S.A., https://doi.org/10.5067/GPMGV/OLYMPEX/PROBES/DATA201, 2018.

Hogan, R. J., Mittermaier, M. P., and Illingworth, A. J.: The retrieval of ice water content from radar reflectivity factor and temperature and its use in evaluating a mesoscale model, J. Appl. Meteorol. Clim., 45, 301–317, https://doi.org/10.1175/JAM2340.1, 2006.

Hogan, R. J., Tian, L., Brown, P. R. A., Westbrook, C. D., Heymsfield, A. J., and Eastment, J. D.: Radar Scattering from Ice Aggregates Using the Horizontally Aligned Oblate Spheroid Approximation, J. Appl. Meteorol. Clima., 51, 655–671, https://doi.org/10.1175/jamc-d-11-074.1, 2012.

Holoborodko, P.: Smooth Noise Robust Differentiators, http://www.holoborodko.com/pavel/numerical-methods/numerical-derivative/smooth-low-noise-differentiators/ (last access: 5 April 2023), 2008.

Houze, R. A., Wurman, J., Brodzik, S., and Framback, A.: GPM Ground Validation Doppler on Wheels (DOW) OLYMPEX V2, NASA EOSDIS Global Hydrology Resource Center Distributed Active Archive Center (DAAC) [data set], Huntsville, Alabama, U.S.A., https://doi.org/10.5067/GPMGV/OLYMPEX/DOW/DATA201, 2018.

Houze Jr., R. A., McMurdie, L. A., Petersen, W. A., Schwaller, M. R., Baccus, W., Lundquist, J. D., Mass, C. F., Nijssen, B., Rutledge, S. A., Hudak, D. R., Tanelli, S., Mace, G. G., Poellot, M. R., Lettenmaier, D. P., Zagrodnik, J. P., Rowe, A. K., DeHart, J. C., Madaus, L. E., Barnes, H. C., and Chandrasekar, V.: The olympic mountains experiment (OLYMPEX), B. Am. Meteorol. Soc., 98, 2167–2188, https://doi.org/10.1175/BAMS-D-16-0182.1, 2017.

Hu, J. and Ryzhkov, A.: Climatology of the vertical profiles of polarimetric radar variables and retrieved microphysical parameters in continental/tropical MCSs and landfalling hurricanes, J. Geophys. Res.-Atmos., 127, e2021JD035498, https://doi.org/10.1029/2021JD035498, 2022.

Kedzuf, N. J., Chiu, J. C., Chandrasekar, V., Biswas, S., Joshil, S. S., Lu, Y., van Leeuwen, P. J., Westbrook, C., Blanchard, Y., and

O'Shea, S.: Retrieving microphysical properties of concurrent pristine ice and snow using polarimetric radar observations, Atmos. Meas. Tech., 14, 6885–6904, https://doi.org/10.5194/amt-14-6885-2021, 2021.

Kumjian, M. R., Mishra, S., Giangrande, S. E., Toto, T., Ryzhkov, A. V., and Bansemer, A.: Polarimetric radar and aircraft observations of saggy bright bands during MC3E, J. Geophys. Res.-Atmos., 121, 3584–3607, https://doi.org/10.1002/2015JD024446, 2016.

Lawson, R. P., O'Connor, D., Zmarzly, P., Weaver, K., Baker, B., Mo, Q., and Jonsson, H.: The 2D-S (Stereo) Probe: Design and Preliminary Tests of a New Airborne, High-Speed, High-Resolution Particle Imaging Probe, J. Atmos. Ocean. Tech., 23, 1462–1477, https://doi.org/10.1175/JTECH1927.1, 2006.

Leinonen, J. and Szyrmer, W.: Radar signatures of snowflake riming: A modeling study, Earth and Space Science, 2, 346–358, https://doi.org/10.1002/2015EA000102, 2015.

Maahn, M., Löhnert, U., Kollias, P., Jackson, R. C., and McFarquhar, G. M.: Developing and evaluating ice cloud parameterizations for forward modeling of radar moments using in situ aircraft observations, J. Atmos. Ocean. Tech., 32, 880–903, https://doi.org/10.1175/JTECH-D-14-00112.1, 2015.

Matrosov, S., Ryzhkov, A., Hardin, J., Shupe, M., Maahn, M., de Boer, G., and Uttal, T.: Intercomparisons of CloudSat and ground-based radar measurements during satellite overpasses, in: 39th Int. Conf. on Radar Meteorology, 16–20 September 2019, Nara, Japan, Amer. Meteor. Soc., 11A-02, https://cscenter.co.jp/icrm2019/program/data/abstracts/Session11A-02_2.pdf (last access: 5 April 2023), 2019.

Matrosov, S. Y., Ryzhkov, A. V., Maahn, M., and De Boer, G.: Hydrometeor shape variability in snowfall as retrieved from polarimetric radar measurements, J. Appl. Meteorol. Clim., 59, 1503–1517, https://doi.org/10.1175/JAMC-D-20-0052.1, 2020.

McMurdie, L., Heymsfield, G., Yorks, J., and Braun, S.: Investigation of Microphysics and Precipitation for Atlantic Coast-Threatening Snowstorms (IMPACTS) Collection, NASA EOSDIS Global Hydrology Resource Center Distributed Active Archive Center [data set], Huntsville, Alabama, U.S.A., https://doi.org/10.5067/IMPACTS/DATA101, 2019.

Moser, M., Voigt, C., Jurkat-Witschas, T., Hahn, V., Mioche, G., Jourdan, O., Dupuy, R., Gourbeyre, C., Schwarzenboeck, A., Lucke, J., Boose, Y., Mech, M., Borrmann, S., Ehrlich, A., Herber, A., Lüpkes, C., and Wendisch, M.: Microphysical and thermodynamic phase analyses of Arctic low-level clouds measured above the sea ice and the open ocean in spring and summer, Atmos. Chem. Phys. Discuss. [preprint], https://doi.org/10.5194/acp-2023-44, in review, 2023.

Murphy, A. M., Ryzhkov, A., and Zhang, P.: Columnar vertical profile (CVP) methodology for validating polarimetric radar retrievals in ice using in situ aircraft measurements, J. Atmos. Ocean. Tech., 37, 1623–1642, https://doi.org/10.1175/JTECH-D-20-0011.1, 2020.

Nguyen, C. M., Wolde, M., and Korolev, A.: Determination of ice water content (IWC) in tropical convective clouds from X-band dual-polarization airborne radar, Atmos. Meas. Tech., 12, 5897–5911, https://doi.org/10.5194/amt-12-5897-2019, 2019.

Petersen, W., Houze, R., and McMurdie, L.: GPM Ground Validation OLYMPEX Field Campaign Data Collection, NASA EOSDIS Global Hydrology Resource Center Distributed Active Archive Center (DAAC) [data set], Huntsville, Alabama, U.S.A., https://doi.org/10.5067/GPMGV/OLYMPEX/DATA101, 2018.

Poellot, M. R., Heymsfield, A. J., and Bansemer, A.: GPM Ground Validation UND Citation Cloud Microphysics OLYMPEX, NASA EOSDIS Global Hydrology Resource Center Distributed Active Archive Center (DAAC) [data set], Huntsville, Alabama, U.S.A., https://doi.org/10.5067/GPMGV/OLYMPEX/MULTIPLE/DATA201, 2017.

Praz, C., Ding, S., McFarquhar, G. M., and Berne, A.: A versatile method for ice particle habit classification using airborne imaging probe data, J. Geophys. Res.-Atmos., 123, 13–472, https://doi.org/10.1029/2018JD029163, 2018.

Przybylo, V. M., Sulia, K. J., Schmitt, C. G., and Lebo, Z. J.: Classification of cloud particle imagery from aircraft platforms using convolutional neural networks, J. Atmos. Ocean. Tech., 39, 405–424, https://doi.org/10.1175/JTECH-D-21-0094.1, 2022.

Reimann, L., Simmer, C., and Trömel, S.: Dual-polarimetric radar estimators of liquid water content over Germany, Meteorol. Z., 30, 237–249, https://doi.org/10.1127/metz/2021/1072, 2021.

Ryzhkov, A., Zhang, P., Reeves, H., Kumjian, M., Tschallener, T., Trömel, S., and Simmer, C.: Quasi-vertical profiles—A new way to look at polarimetric radar data, J. Atmos. Ocean. Tech., 33, 551–562, https://doi.org/10.1175/JTECH-D-15-0020.1, 2016.

Ryzhkov, A., Bukovcic, P., Murphy, A., Zhang, P., and McFarquhar, G.: Ice microphysical retrievals using polarimetric radar data, in: 10th European Conference on Radar in Meteorology and Hydrology, 1–6 July 2018, the Netherlands, 494–504, https://doi.org/10.18174/454537, 2018.

Ryzhkov, A. V. and Zrnić, D. S.: Radar Polarimetry for Weather Observations, vol. 486, Springer, ISBN 978-3-030-05092-4, https://doi.org/10.1007/978-3-030-05093-1, 2019.

Ryzhkov, A. V., Zrnic, D. S., and Gordon, B.: Polarimetric method for ice water content determination, J. Appl. Meteorol., 37, 125–134, https://doi.org/10.1175/1520-0450(1998)037<0125:PMFIWC>2.0.CO;2, 1998.

Ryzhkov, A. V., Snyder, J., Carlin, J. T., Khain, A., and Pinsky, M.: What polarimetric weather radars offer to cloud modelers: forward radar operators and microphysical/thermodynamic retrievals, Atmosphere, 11, 362, https://doi.org/10.3390/atmos11040362, 2020.

Skofronick-Jackson, G., Hudak, D., Petersen, W., Nesbitt, S. W., Chandrasekar, V., Durden, S., Gleicher, K. J., Huang, G.-J., Joe, P., Kollias, P., Reed, K. A., Schwaller, M. R., Stewart, R., Tanelli, S., Tokay, A., Wang, J. R., and Wolde, M.: Global Precipitation Measurement Cold Season Precipitation Experiment (GCPEX): for measurement's sake, let it snow, B. Am. Meteorol. Soc., 96, 1719–1741, https://doi.org/10.1175/BAMS-D-13-00262.1, 2015.

Skofronick-Jackson, G., Kulie, M., Milani, L., Munchak, S. J., Wood, N. B., and Levizzani, V.: Satellite estimation of falling snow: A global precipitation measurement (GPM) core observatory perspective, J. Appl. Meteorol. Clim., 58, 1429–1448, https://doi.org/10.1175/JAMC-D-18-0124.1, 2019.

Tian, J., Dong, X., Xi, B., Wang, J., Homeyer, C. R., McFarquhar, G. M., and Fan, J.: Retrievals of ice cloud microphysical properties of deep convective systems using radar measurements, J. Geophys. Res.-Atmos., 121, 10820–10839, https://doi.org/10.1002/2015JD024686, 2016.

Tobin, D. M. and Kumjian, M. R.: Polarimetric radar and surface-based precipitation-type observations of ice pellet to freezing rain transitions, Weather Forecast., 32, 2065–2082, https://doi.org/10.1175/WAF-D-17-0054.1, 2017.

Tridon, F., Battaglia, A., Chase, R. J., Turk, F. J., Leinonen, J., Kneifel, S., Mroz, K., Finlon, J., Bansemer, A., Tanelli, S., Heymsfield, A. J., and Nesbitt, S. W.: The microphysics of stratiform precipitation during OLYMPEX: Compatibility between triple-frequency radar and airborne in situ observations, J. Geophys. Res.-Atmos., 124, 8764–8792, https://doi.org/10.1029/2018JD029858, 2019.

Trömel, S., Simmer, C., Blahak, U., Blanke, A., Doktorowski, S., Ewald, F., Frech, M., Gergely, M., Hagen, M., Janjic, T., Kalesse-Los, H., Kneifel, S., Knote, C., Mendrok, J., Moser, M., Köcher, G., Mühlbauer, K., Myagkov, A., Pejcic, V., Seifert, P., Shrestha, P., Teisseire, A., von Terzi, L., Tetoni, E., Vogl, T., Voigt, C., Zeng, Y., Zinner, T., and Quaas, J.: Overview: Fusion of radar polarimetry and numerical atmospheric modelling towards an improved understanding of cloud and precipitation processes, Atmos. Chem. Phys., 21, 17291–17314, https://doi.org/10.5194/acp-21-17291-2021, 2021.

Ulbrich, C. W.: Natural variations in the analytical form of the raindrop size distribution, J. Appl. Meteorol. Clim., 22, 1764–1775, 1983.

Vogel, J. M. and Fabry, F.: Contrasting polarimetric observations of stratiform riming and nonriming events, J. Appl. Meteorol. Clim., 57, 457–476, https://doi.org/10.1175/JAMC-D-16-0370.1, 2018.

Vulpiani, G., Montopoli, M., Passeri, L. D., Gioia, A. G., Giordano, P., and Marzano, F. S.: On the use of dual-polarized C-band radar for operational rainfall retrieval in mountainous areas, J. Appl. Meteorol. Clim., 51, 405–425, https://doi.org/10.1175/JAMC-D-10-05024.1, 2012.

Wurman, J., Straka, J., Rasmussen, E., Randall, M., and Zahrai, A.: Design and deployment of a portable, pencil-beam, pulsed, 3-cm Doppler radar, J. Atmos. Ocean. Tech., 14, 1502–1512, https://doi.org/10.1175/1520-0426(1997)014<1502:DADOAP>2.0.CO;2, 1997.

Zängl, G., Reinert, D., Rípodas, P., and Baldauf, M.: The ICON (ICOsahedral Non-hydrostatic) modelling framework of DWD and MPI-M: Description of the non-hydrostatic dynamical core, Q. J. Roy. Meteor. Soc., 141, 563–579, https://doi.org/10.1002/qj.2378, 2015.